Numerical simulation of wetting phenomena by a meshfree particle method

Sudarshan Tiwari*,[a], Axel Klar[b], Steffen Hardt[c]

[a] *Fachbereich Mathematik, TU Kaiserslautern, Gottlieb-Daimler-Strasse, 67663 Kaiserslautern, Germany*
[b] *Fachbereich Mathematik, TU Kaiserslautern, Gottlieb-Daimler-Strasse, 67663 Kaiserslautern, Germany*
Fraunhofer ITWM Kaiserslautern, 67663 Kaiserslautern, Germany
[c] *Center of Smart Interfaces, TU Darmstadt, Alarich-Weiss-Str. 10, 64287, TU Darmstadt Germany*

Abstract

Simulations of wetting phenomena by a meshfree particle method are presented. The incompressible Navier-Stokes equations are used to model the two-phase flow. The continuous surface force model is used to incorporate the surface tension force. Chorin's projection method is applied to discretize the Navier-Stokes equations. The different fluid phases are identified by assigning different colors and different material properties (density, viscosity) to the particles that remain unchanged throughout a simulation. Two-phase flow is captured by a one-fluid model via using weighted averages of the density and viscosity in a region around the fluid-fluid interface. The differential operators at each particle are computed from the surrounding cloud of particles with the help of the least-squares method. The numerical results are compared with specific analytical solutions, but also with previously considered test cases involving wetting of a container and sessile drops. A good overall agreement is found.

Key words: two-phase flow, meshfree particle method, wetting, contact angle

*Corresponding Author
Email addresses: tiwari@mathematik.uni-kl.de (Sudarshan Tiwari), klar@mathematik.uni-kl.de (Axel Klar), hardt@csi.tu-darmstadt.de (Steffen Hardt)

1. Introduction

Surface-tension driven flows occur when the surface-tension forces acting on a liquid are of equal or even larger magnitude than the inertial, viscous or gravitational forces. There exist numerous applications in which such flows are important, for example in the areas of microfluidics [20], [22], coating technology [29], two-phase heat transfer [8] or oil recovery [2], [3]. Correspondingly, there is a high demand for efficient numerical models and schemes to compute surface-tension driven flows.

In the past decades, a large number of CFD approaches have been presented that explicitly resolve the interface between two immiscible fluids. Often these are classified either as interface-tracking or interface-capturing schemes. In the former, the time evolution of the interface is represented by the time evolution of the numerical grid whose structure contains information about the interface shape. In the latter, the evolution of the interface is decoupled from the grid. Instead, the interface is reconstructed from field quantities represented on the grid. The most popular examples of interface capturing schemes are probably the volume-of-fluid [10]and the level-set method [21]. While interface-tracking schemes tend to be very accurate, they are not well suited to study flows with topological changes occurring when, for example, drops or liquid sheets break up or merge. For the latter, interface capturing schemes are suitable candidates.

The past decades, fast progress has been made in the development of particle-based or meshfree methods to compute various types of flows. In such schemes Lagrangian particles, serving as the basic building blocks for discretization of the fluid dynamic equations, are advected with the flow. This has the advantage of a certain degree of inherent adaptivity, i.e. the numerical resolution is provided only where it is needed. Classical examples for the application of meshfree methods are astrophysical flows [18] in which the set of Lagrangian particles co-evolves with an astrophysical structure, e.g. a plasma cloud. Often, in gas-liquid flows a similar division in an important and an unimportant subdomain occurs. Compared to the liquid, the stresses in the gas phase are often negligible,

which means that it is sufficient to compute the flow in the liquid phase alone. Meshfree methods lend themselves for this purpose. Furthermore, in contrast to interface-tracking schemes, meshfree methods easily allow studying free-surface flows with topological changes. In total, meshfree methods appear to be ideal candidates for the simulation of complex gas-liquid flows. Among these, surface-tension driven flows form an important subclass.

The first meshfree Lagrangian method that has been formulated to solve fluid dynamics equations is denoted Smooothed Particle Hydrodynamics (SPH) [9]. Another meshfree Lagrangian CFD approach is the moving particle semi-implicit method [13]. In this article we use a meshfree particle method, called Finite Pointset Method (FPM), to solve the incompressible Navier-Stokes equations. FPM is a fully Lagrangian particle method and has similar character as the SPH method except for the approximation of spatial derivatives and the treatment of boundary conditions. In SPH the spatial derivatives at an arbitrary particle position are approximated by an interpolation approach from the surrounding particles. However, in FPM the spatial derivatives are approximated using the finite-difference approach [24], where the spatial differential operators at an arbitrary particle position are approximated by the moving least squares approach [6]. The Poisson equation for the pressure field is also solved in the sense of constrained least squares. The domain boundaries are represented by boundary particles, and boundary conditions are directly prescribed on those particles.

Meshfree particle methods are appropriate tools to simulate surface-tension driven flows. Each phase is indicated by the color of the respective particles. When particles move, they carry all the information about the flow with them such as their color, density, velocity, etc. The colors, densities and viscosity values of all particles remain constant during the time evolution. The fluid-fluid interface is easily determined with the help of the color function. To the best of the author's knowledge, the first implementation of the continuous surface force (CSF) model to account for surface-tension forces was presented in [19]. In [26] an implementation of the CSF model within the FPM was presented to

simulate surface-tension driven flows. The present article is an extension of [26], devoted to studying wetting phenomena.

The paper is organized as follows. In section 2 we present the mathematical model and the numerical scheme. In section 3 some specific aspects of the FPM are presented. The numerical test cases are presented in section 4. In some cases analytical solutions can be calculated, and the numerical solutions are compared with the analytical ones. In those cases where analytical solutions are not known, the results are compared to numerical results published earlier. Moreover, some convergence studies are presented in section 4. The paper finishes with concluding remarks and suggestions for future work.

2. Mathematical model and numerical scheme

2.1. Mathematical model

We consider two immiscible fluids, for example, liquid and gas, where both of them are incompressible. We use the one fluid formulation of two-phase flows from [4]. We model the two-phase flows by the incompressible Navier-Stokes equations. The equations are expressed in the Lagrangian form

$$\frac{d\vec{x}}{dt} = \vec{v} \tag{1}$$

$$\nabla \cdot \vec{v} = 0 \tag{2}$$

$$\frac{D\vec{v}}{Dt} = -\frac{1}{\rho}\nabla p + \frac{1}{\rho}\nabla \cdot (2\mu D) + \vec{g} + \frac{1}{\rho}\vec{F}_S, \tag{3}$$

where $\vec{v}$ is the fluid velocity vector, ρ is the density, μ is the dynamic viscosity, D is the viscous stress tensor $D = \frac{1}{2}(\nabla\vec{v} + \nabla^T\vec{v})$, $\vec{g}$ is the gravitational acceleration and $\vec{F}_S$ is the surface tension force. In general, ρ and μ are discontinuous across the interface and remain constant in each phase. The surface tension force $\vec{F}_S$ is computed using the classical continuum surface force (CSF) model [4]. It acts on the vicinity of the interface between the fluids. In the CSF model the surface tension force $\vec{F}_S$ is defined by

$$\vec{F}_S = \sigma\kappa\vec{n_I}\delta_S, \tag{4}$$

where σ is the surface tension coefficient, assumed to be a constant, κ is the curvature, $\vec{n}_I$ is the unit normal vector of the interface and δ_S is a smeared delta function, peaked at the interface.

The equations (1 - 3) are solved with initial and boundary conditions.

2.2. Computation of the surface tension force

Particle methods are suitable to compute the surface tension force and surface tension driven flows. The interface can accurately predict the flow behaviors, see [19],[26]. The interface can be accurately determined by assigning colors or flags to the particle of each phase. For example, we define the color $c = 1$ for the gas and $c = 2$ for the liquid. The normal vector $\vec{n}_I$ on the interface is computed as the gradient of the color function c. Since c is discontinuous across the interface, one has to smooth it. Let $\vec{x}$ be the position of an arbitrary particle and has neighbors with function values $c_j = c(\vec{x}_j)$. We smooth c at $\vec{x}$ from its neighbors with the help of the Shepard interpolation rule given by

$$\tilde{c}(\vec{x}) = \frac{\sum_{j=1}^{m} w_j c_j}{\sum_{j=1}^{m} w_j} \tag{5}$$

where $\vec{x}$ is an arbitrary particle position, m is the number of neighbors and w_j is the weight function given by

$$w_j = w(\vec{x}_j - \vec{x}; h) = \begin{cases} \exp(-\alpha \frac{\|\vec{x}_j - \vec{x}\|^2}{h^2}), & \text{if } \frac{\|\vec{x}_i - \vec{x}\|}{h} \leq 1 \\ 0, & \text{else,} \end{cases} \tag{6}$$

where α is a positive constant. For more details we refer to section 3. We observe that the gradient of $\tilde{c}$ are non-vanishing only in a region close to the interface. The unit normal vector is computed by

$$\vec{n}_I = \frac{\nabla \tilde{c}}{|\nabla \tilde{c}|}. \tag{7}$$

Furthermore, the curvature is calculated using

$$\kappa = -\nabla \cdot \vec{n}_I. \tag{8}$$

There exist many possible choices for δ_s, but in practice, it is often approximated as

$$\delta_s \approx |\nabla \tilde{c}|. \tag{9}$$

We note that δ_s is non-zero in the viciinity of the interface and zero far from it.

2.3. Boundary conditions

In this paper, we consider the flow in a closed container such that there are no in- and outflow boundaries. We have to deal only with the solid wall and interface boundary conditions. Interface boundary conditions are implicitly taken care by the CSF model, *i. e.* an explicit precription is not necessary. On the solid walls we use kinematic and no-slip boundary conditions, given by

$$\vec{v} \cdot \vec{n} = 0 \quad \text{and} \quad \vec{v} = \vec{0}, \tag{10}$$

where $\vec{n}$ is the unit normal vector on a wall.

In addition to the above boundary conditions, the contact angle of the liquid at the solid wall needs to be prescribed. The contact angle follows from the wetting force, which is the balance between the cohesive forces of the liquid and the adhesive forces between the liquid and the wall. The line of intersection of the three phases is called the contact line. The angle between the gas liquid interface and the solid wall is called the contact angle. In this paper we only prescribe the static contact angle. The equilibrium static contact angle θ_s of a liquid drop on a solid wall determines the wetability. A wetting liquid has a static contact angle less than 90^o, and a non-wetting liquid has a static contact angle larger than 90^o. In this paper we use the method suggested by Brackbill et al [4]. Let $\vec{x}_w$ be a point on the solid wall with outward normal $\vec{n}$. Let $\vec{n}_I$ be the normal on the interface defined by (7). Before computing the curvature from (8) one guarantees that the boundary outward normal $\vec{n}$ makes an angle θ_s with the interface normal $\vec{n}_I$. This means that the following condition must be satisfied

$$\vec{n} \cdot \vec{n}_I = \cos\theta_s \tag{11}$$

Therefore, we redefine the interface normals $\vec{n}_I$ at $\vec{x}_w$ and its nearest neighbors within a radius $\beta\ h$ as

$$\hat{\vec{n}}_I = \vec{n}\cos\theta_s + \vec{n}_{||}\sin\theta_s, \tag{12}$$

where $\vec{n}_{||}$ is the unit vector parallel to the wall normal to the three-phase contact line. One can replace $\vec{n}_{||}$ by $\vec{n}_I$ computed from (7) if the real color distribution in combination with a ghost distribution is used, as described in [4]. The ghost distribution is obtained by reflecting the real distribution at the wall surface. The constant β lies in the interval $(0.6, 1)$ and is problem specific. In our simulations we have used $\beta = 1$. We replace $\vec{n}_I$ by this corrected interface normal in the vicinity of $\vec{x}_w$, then we compute the curvature κ from equation (8).

2.4. Numerical scheme

We consider Chorin's projection method [5] in the framework of a particle method. Let dt be a time step and set $t^n = ndt, n = 0, 1, 2, \ldots$. We denote, for example, $\vec{x}^n$ as the position of a particle at time level n. Chorin's projection scheme consists of two steps, where in the first step we compute the intermediate velocity $\vec{v}^*$ explicetely from the momentum equation without pressure term

$$\vec{v}^* = \vec{v}^n + \frac{dt}{\rho}\nabla \cdot (2\mu D^n) + dt\vec{g} + \frac{dt}{\rho}\vec{F}_S^n. \tag{13}$$

Due to the Lagrangian formulation we do not have to deal with the nonlinear convective term. In the second step, called the projection step, we compute the velocity at time level $(n + 1)$ by solving the equation

$$\vec{v}^{n+1} = \vec{v}^* - dt\ \frac{\nabla p^{n+1}}{\rho} \tag{14}$$

with the constraint that $\vec{v}^{n+1}$ satisfies the continuity equation

$$\nabla \vec{v}^{n+1} = 0. \tag{15}$$

In order to compute $\vec{v}^{n+1}$ we need the knowledge of p^{n+1}. This is obtained by taking the divergence of equation (14) and making use of the constraint (15). Then we get the Poisson equation for the pressure

$$\nabla \cdot \left(\frac{\nabla p^{n+1}}{\rho} \right) = \frac{\nabla \cdot \vec{v}^*}{dt}. \tag{16}$$

The boundary condition for p is obtained by projecting equation (14) on the outward unit normal vector $\vec{n}$ at the boundary Γ. Thus, we obtain the Neumann boundary condition

$$\left(\frac{\partial p}{\partial \vec{n}}\right)^{n+1} = -\frac{\rho}{dt}(\vec{v}_\Gamma^{n+1} - \vec{v}_\Gamma^{*}) \cdot \vec{n}, \tag{17}$$

where $\vec{v}_\Gamma$ is the value of $\vec{v}$ on Γ. Assuming $\vec{v} \cdot \vec{n} = 0$ on Γ, we obtain

$$\left(\frac{\partial p}{\partial \vec{n}}\right)^{n+1} = 0 \tag{18}$$

on Γ.

In addition, we compute the new particle positions at the $(n+1)$th level by

$$\vec{x}^{n+1} = \vec{x}^{n} + dt\ \vec{v}^{n}. \tag{19}$$

The numerical implementation of the above scheme requires the computation of the first and second order partial derivatives at every particle position. The spatial partial derivatives at an arbitrary particle are approximated from its neighboring cloud of particles with the help of the weighted least squares method, described in section 3. Next, we have to solve the Poisson equation for the pressure (16). After smoothing of the interface as described above, the coefficient $1/\rho$ of the Poisson equation is smooth, but strongly varying near the interface. The same holds for the viscosity in equation (13) for $\vec{v}^*$. The smoothing process is similar to the smoothing of the color function. However, we have to iterate the iteration process more times if the density and viscosity have higher ratios like $1000 : 1$ and $100 : 1$, respectively. Otherwise, the scheme becomes unstable. After smoothing the density, equation (16) can be re-expressed as

$$-\frac{\nabla \tilde{\rho}}{\tilde{\rho}} \cdot \nabla p^{n+1} + \Delta p^{n+1} = \tilde{\rho}\frac{\nabla \cdot \vec{v}^{*}}{dt}, \tag{20}$$

where $\tilde{\rho}$ is the smoothed density. Note that, for constant density the first term of (20) vanishes and we get the pressure Poisson equation. Far from the interface we have $\tilde{\rho} = \rho$. In the following section we describe the method of solving equations of type (20) by a meshfree particle method, called the Finite Pointset Method (FPM).

3. Finite Pointset Method (FPM)

FPM is a Lagrangian meshfree particle method. It has been successfully used to simulate compressible as well as incompressible flows, see [14], [24] and references there in. Also it has been extended to free-surface and two-phase flows [25], [26]. In the following subsections we present a brief description of the method.

3.1. Approximation of spatial derivatives

In this paper we limit ourselves to a two-dimensional spatial domain. The extension of the method to three-dimensional space is straightforward. Consider the computational domain $\Omega \in R^2$. Approximate Ω by particles $\vec{x}_i, i = 1, \ldots, N$, whose distribution can be quite irregular. These particles serve as numerical grid points. Let $\psi(\vec{x})$ be a scalar function and $\psi_i = \psi(\vec{x}_i)$ its values for $i = 1, \ldots, N$. We consider the problem to approximate the spatial derivatives at an arbitrary point $\vec{x} \in \{\vec{x}_i, i = 1, \ldots, N\}$, in terms of the values of a set of its neighboring points. In order to restrict the number of neighboring points we define a weight function $w = w(\vec{x}_i - \vec{x}, h)$ with small compact support of size h. The size of h has to be chosen such that we have at least a minimum number of particles, for example, in $2D$, we need at least 5 neighboring particles. In practice we define h as 2.5 to 3 times the initial spacing of particles, keeping in mind that this is a user defined factor. The weight function can be quite arbitrary. In our case we consider the Gaussian weight function defined in (6), where α is equal to 6.25. Let $P(\vec{x}, h) = \{\vec{x}_j : j = 1, 2, \ldots, m\}$ be the set of m neighboring points of $\vec{x}$ in a circle of radius h.

Consider m Taylor expansions of $\psi(\vec{x}_i)$ around $\vec{x} = (x, y)$

$$\psi(x_j, y_j) = \psi(x, y) + \frac{\partial \psi}{\partial x}(x_j - x) + \frac{\partial \psi}{\partial y}(y_j - y) + \frac{1}{2}\frac{\partial^2 \psi}{\partial x^2}(x_j - x)^2 + \frac{\partial^2 \psi}{\partial x \partial y}(x_j - x)(y_j - y) + \frac{1}{2}\frac{\partial^2 \psi}{\partial y^2}(y_j - y)^2 + e_j \qquad (21)$$

for $j = 1, \ldots, m$, where e_j is the residual error. Denote the coefficients

$$a_0 = \psi(x,y),\ a_1 = \frac{\partial \psi}{\partial x},\ a_2 = \frac{\partial \psi}{\partial y},$$
$$a_3 = \frac{\partial^2 \psi}{\partial x^2},\ a_4 = \frac{\partial^2 \psi}{\partial x \partial y}, a_5 = \frac{\partial^2 \psi}{\partial y^2}.$$

Note that a_0 is known, so we have five unknowns $a_i, i = 1, \ldots, 5$. Now we have to solve m equations for five unknowns . For $m > 5$ this system is overdetermined and can be written in matrix form as

$$\vec{e} = M\vec{a} - \vec{b}, \tag{22}$$

where $M =$

$$\begin{pmatrix} dx_1 & dy_1 & \frac{1}{2}dx_1^2 & dx_1 dy_1 & \frac{1}{2}dy_1^2 \\ \vdots & \vdots & \vdots & \vdots & \vdots \\ dx_m & dy_m & \frac{1}{2}dx_m^2 & dx_m dy_m & \frac{1}{2}dy_m^2 \end{pmatrix} \tag{23}$$

$\vec{a} = (a_1, a_2, \ldots a_5)^T$, $\vec{b} = (\psi_1 - a_0, \ldots, \psi_m - a_0)^T$, $\vec{e} = (e_1, \ldots, e_m)^T$ and $dx_j = x_j - x,\ dy_j = y_j - y$.

The unknowns a_i are computed by minimizing a weighted error over the neighboring points. Thus, we have to minimize the following quadratic form

$$J = \sum_{i=1}^{m} w_i e_i^2 = (M\vec{a} - \vec{b})^T W (M\vec{a} - \vec{b}), \tag{24}$$

where

$$W = \begin{pmatrix} w_1 & 0 & \cdots & 0 \\ \vdots & \vdots & \ldots & \vdots \\ 0 & 0 & \cdots & w_m \end{pmatrix}.$$

The minimization of J with respect to $\vec{a}$ formally yields (if $M^T W M$ is nonsingular)

$$\vec{a} = (M^T W M)^{-1} (M^T W)\vec{b}. \tag{25}$$

3.2. Particle method for solving the Poisson equation

With equation (20) we have to solve a linear partial differential of second order of the form

$$\vec{B} \cdot \nabla \psi + C \Delta \psi = f, \tag{26}$$

where $\vec{B}, C$ and f are given. The equation is solved with Dirichlet or Neumann boundary conditions

$$\psi = g \qquad \text{or} \quad \frac{\partial \psi}{\partial \vec{n}} = \phi. \tag{27}$$

In fact, we can substitute the partial differential operators appearing in equation (26) by the components of a from equation (25). This approach was first proposed in [16]. However, it has some difficulties when dealing with the Neumann boundary condition. In the following we describe a meshfree particle method, initially proposed in [23], which is more stable compared to the method given in [16] (see [12] for details). Moreover, the method can easily handle the Neumann boundary condition and has a second-order convergence.

We consider again an arbitrary particle position (x, y) having m neighbors, as in subsection 3.1. We reconsider the m Taylor expansions of equation (21). We add the constraint that at particle position (x, y) the partial differential equation (26) should be satisfied. If the point (x, y) lies on the boundary, also the boundary condition (27) needs to be satiesfied. Therefore, we add the equations (26) and (27) to these m equations (21). Equations (26) and (27) are re-expressed as

$$B_1 a_1 + B_2 a_2 + C(a_3 + a_5) = f \tag{28}$$

$$n_x a_1 + n_y a_2 = \phi, \tag{29}$$

where n_x, n_y are the x, y components of the unit normal vector $\vec{n}$ on the boundary Γ.

In this formulation the function values $\psi(x, y)$ are not known a priori, therefore, the term a_0 is also unknown. In total we have six unknowns $a_i, i = 0, 1, \ldots, 5$. For the interior particles we add equation (28), and for boundary particles with Neumann boundary conditions equation (29) as constraints. Now we have to solve $m+1$ equations for six unknowns. For $m+1 > 6$ this system is overdetermined with respect to the unknowns a_i and can be written in matrix

form (36), where the matrix M differs from (23) and is given by

$$\begin{pmatrix} 1 & dx_1 & dy_1 & \frac{1}{2}dx_1^2 & dx_1dy_1 & \frac{1}{2}dy_1^2 \\ \vdots & \vdots & \vdots & \vdots & \vdots & \vdots \\ 1 & dx_m & dy_m & \frac{1}{2}dx_m^2 & dx_mdy_m & \frac{1}{2}dy_m^2 \\ 0 & B_1 & B_2 & C & 0 & C \\ 0 & n_x & n_y & 0 & 0 & 0 \end{pmatrix}, \tag{30}$$

where $\vec{a} = (a_0, a_1, \ldots a_5)^T$, $\vec{b} = (\psi_1, \ldots, \psi_m, f, g)^T$ and $\vec{e} = (e_1, \ldots, e_m, e_{m+1}, e_{m+2})^T$. From a programming point of view, we set $n_x = n_y = 0$ for the interior particles. For the Dirichlet boundary particles, we directly prescribe the boundary conditions, and for the Neumann boundary particles we set $B_1 = B_2 = C = 0$ and $f = 0$.

Similarly, the unknowns a_i are computed by minimizing a weighted error function and obtained in the form (25). In (25) the vector $(M^TW)\vec{b}$ is explicitely given by

$$\begin{aligned}(M^TW)\vec{b} = \Bigg(&\sum_{j=1}^{m} w_j\psi_j,\ \sum_{j=1}^{m} w_j dx_j\psi_j + B_1 f + n_x\phi, \\ &\sum_{j=1}^{m} w_j dy_j\psi_j + B_2 f + n_y\phi,\ \frac{1}{2}\sum_{j=1}^{m} w_j dx_j^2\psi_j + Cf, \\ &\sum_{j=1}^{m} w_j dx_j dy_j\psi_j,\ \frac{1}{2}\sum_{j=1}^{m} w_j dy_j^2\psi_j + Cf\Bigg)^T. \end{aligned} \tag{31}$$

Equating the first components on both sides of equation (25), we get

$$\begin{aligned}\psi = Q_1\left(\sum_{j=1}^{m} w_j\psi_j\right) + Q_2\left(\sum_{j=1}^{m} w_j dx_j\psi_j + B_1 f + n_x\phi\right) + \\ Q_3\left(\sum_{j=1}^{m} w_j dy_j\psi_j + B_2 f + n_y\phi\right) + Q_4\left(\frac{1}{2}\sum_{j=1}^{m} w_j dx_j^2\psi_j + Cf\right) + \\ Q_5\left(\sum_{j=1}^{m} w_j dx_j dy_j\psi_j\right) + Q_6\left(\frac{1}{2}\sum_{j=1}^{m} w_j dy_j^2\psi_j + Cf\right), \end{aligned} \tag{32}$$

where $Q_1, Q_2, \ldots, Q_6$ are the components of the first row of the matrix $(M^T W M)^{-1}$. Rearranging the terms, we have

$$\psi - \sum_{j=1}^{m} w_j \left(Q_1 + Q_2 dx_j + Q_3 dy_j + Q_4 \frac{dx_j^2}{2} + Q_5 dx_j \; dy_j + Q_6 \frac{dy_j^2}{2} \right) \psi_j = \\ (Q_2 B_1 + Q_3 B_2 + Q_4 C + Q_6 C) \, f + (Q_2 n_x + Q_3 n_y) \, \phi. \tag{33}$$

Equation (33) is for an arbitrary particle $\vec{x}$, which is one of the particle $\vec{x}_i, i = 1, \ldots, N$, having $m(i)$ neighbors at $\vec{x}_{i_j}$. We repeat the computation of equation (33) for all particles $i = 1, \ldots, N$, giving the following sparse linear system of equations for the unknowns $\psi_i, i = 1, \ldots, N$

$$\psi_i - \sum_{j=1}^{m(i)} w_{i_j} \left(Q_1 + Q_2 dx_{i_j} + Q_3 dy_{i_j} + Q_4 \frac{dx_{i_j}^2}{2} + Q_5 dx_{i_j} dy_{i_j} + Q_6 \frac{dy_{i_j}^2}{2} \right) \psi_{i_j} = \\ (Q_2 B_1 + Q_3 B_2 + Q_4 C + Q_6 C) \, f_i + (Q_2 n_x + Q_3 n_y) \, \phi_i. \tag{34}$$

In the matrix form we have

$$L \vec{\Psi} = \vec{R}, \tag{35}$$

where $\vec{R}$ is the right-hand side vector, $\vec{\Psi}$ is the unknown vector and L is the sparse matrix having non-zero entries only for neighboring particles.

The sparse system (35) can be solved by some iterative methods. In this paper we apply the method of Gauss-Seidel. In the projection scheme it is also necessary to prescribe initial values for the pressure at time $t = 0$. For example, we can prescribe a vanishing pressure initially. Then, in the time iteration the initial values of the pressure for time step $n + 1$ are taken as the values from time step n. Usually, solving the pressure Poisson equation will require more iterations in the first few time steps. After a certain number of time steps, the pressure values at the old time step are close to those of new time step, so the number of iterations required gets reduced.

The iteration process is stopped if the relative error satisfies

$$\frac{\sum_{i=1}^{N} |\psi_i^{\tau+1} - \psi_i^{(\tau)}|}{\sum_{i=1}^{N} |\psi_i^{(\tau+1)}|} < \epsilon, \tag{36}$$

where $\tau = 0, 1, 2, \ldots$, and the approximation to the solution is defined by $\psi(\vec{x}_i) := \psi^{(\tau+1)}(\vec{x}_i), i = 1, \ldots, N$. The parameter ϵ is a small positive constant

and can be defined by the user. The required number of iterations depends on the values of ϵ and h.

4. Numerical tests

4.1. Elliptic equation

As a first numerical test we study the diffusion equation

$$\nabla \cdot (k \nabla \psi) = f \quad \text{in} \quad \Omega, \tag{37}$$

where k is smooth, but strongly varying near the interface. Away from the interface we have

$$k = \begin{cases} k_1 \text{ in } \Omega_1 \\ k_2 \text{ in } \Omega_2 \end{cases}$$

with $k_1 \neq k_2$ and $\Omega = \Omega_1 \cup \Omega_2$. Equation (37) is similar to the pressure Poisson equation in the projection step, therefore, the accuracy of its solution is very important for our numerical scheme. For the sake of simplicity, we consider Dirichlet boundary conditions. In the following we study the numerical solution for two examples with different interfaces between the two subdomains, compare [12]. We monitor the error between the numerical solution of the above problem with smoothed coefficient and the exact solution of the problem with discontinuous coefficients given by the above two constants in the respective domains. For the latter problem we have to prescribe additional conditions at the interface, i.e. the continuity of the solution and normal component of the flux through the interface.

4.1.1. Example 1

Let $\Omega = [0,1] \times [0,1]$ an unit square and decompose it into two domains with interface $x = 0.5$. Consider $k = k_1 = 1000$ for $x \leq 0.5$ and $k = k_2 = 1$ for $x > 0.5$. Using $k = k_1$ and $k = k_2$ respectively, we define in the two domains

$$\varphi(x,y) = \frac{1}{k} \sin(\frac{\pi x}{2})(x - \frac{1}{2})(y - \frac{1}{2})(1 + x^2 + y^2). \tag{38}$$

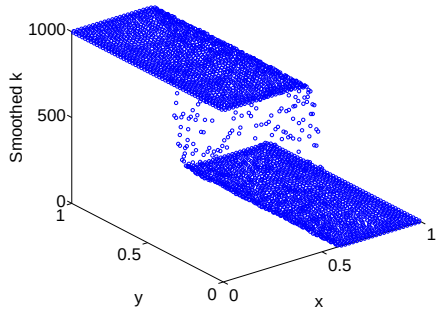

Figure 1: Smoothed value of diffusion coefficient k

Then, we consider a source term f given in each of the domains by

$$f = \nabla \cdot (k \nabla \varphi) \,. \tag{39}$$

The Dirichlet boundary conditions are given by the values of φ on the boundary. Obviously, the exact solution of (37) with discontinuous coefficients given by the two constants in the respective domains is given by

$$\psi = \varphi. \tag{40}$$

We note that solution and flux are continuous at the interface. This solution is compared to the numerical solution of (37) with a smoothed diffusion coefficient. In Fig. 1 we have plotted the smoothed values of k. We iterate the smoothing process three times using the Shepard interpolation rule (5). In Fig. 2 we show the exact and numerical solutions for $h = 0.04$, which corresponds to a total number of particles equal to 3417. Furthermore, we have performed a convergence study, see Table 1, where we plot the maximum error between the exact solution with discontinuous k and the numerical solutions with smoothed k. We observe that the order of convergence is approximately one. In this case, using the smoothing of the coefficent near the interface reduces the order of convergence from two to one.

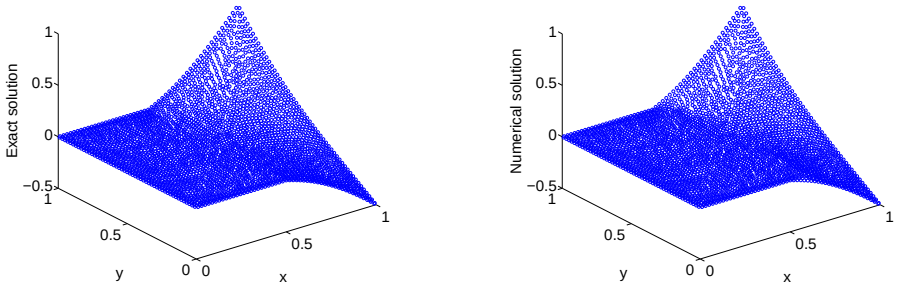

Figure 2: Left: exact solution and right: numerical solution for example 1.

h	N	L^∞ error
0.08	909	1.284×10^{-1}
0.04	3222	6.7518×10^{-2}
0.02	13177	3.5763×10^{-2}
0.01	52089	1.8636×10^{-2}

Table 1: Convergence study for example 1

h	N	L^∞ error
0.08	909	3.272×10^{-1}
0.04	3222	1.186×10^{-1}
0.02	13177	4.3195×10^{-2}
0.01	52089	1.7366×10^{-2}

Table 2: Convergence study for example 2

4.1.2. Example 2

Again we consider the unit square as a computational domain. We again decompose the domain into two parts. However, the interface is now defined as an ellipse

$$(x - \frac{1}{2})^2 + 4(y - \frac{1}{2})^2 = r^2, \tag{41}$$

where $r = 0.1$. We consider $k = 1000$ inside the ellipse and $k = 1$ elsewhere. The manufactured solution for the problem with discontinuous diffusion coefficient is given by

$$\psi(x, y) = \varphi(x, y) = \frac{1}{k} \sin(\frac{\pi x}{2}) \left[(x - \frac{1}{2})^2 + 4(y - \frac{1}{2})^2 - r^2 \right] (1 + x^2 + y^2). \tag{42}$$

The maximum error between the exact solution with discontinuous coefficient and the numerical solutions of the problem with smoothed coefficient can be found in Table 2. The errors in Table 2 show again first order convergence.

4.2. Flow induced by wall adhesion

The following test cases of flows induced by wall adhesion have been analyzed by Brackbill et al [4] and later by Liu et al [15]. We consider a shallow pool of water located at the bottom and gas at the top of a two-dimensional tank of size $[0, 0.112] \times [0, 0.152]$. Two different cases for the equilibrium contact angle are studied, $\theta_s = 175^o$ and 5^o. $\theta_s = 5^o$ corresponds to the wetting situation and $\theta_s = 175^o$ to a non-wetting one. The following material parameters are chosen for both cases: $\rho_l = 1000$ kg m^{-3}, $\mu_l = 0.0091$ Pa s for the liquid, $\rho_g = 1$ kg m^{-3}, $\mu_g = 1.86 \times 10^{-5}$ Pa s for the gas, and $\sigma = 0.072$ Nm^{-1}. The

external forces, for example, the gravity force, are set to zero. The initial spacing of the particles is approximately $\Delta x \approx h/3$, where $h = 0.004$, which gives an initial total number of particles equal to 5737. A fixed time step $dt = 0.0002$ is chosen. During a time step, we have to add particles if they leave a void and remove them if they are very close to each other. If two particles are very close to each other, we replace the new one at the mean position and delete the two closed particles. The fluid quantities are assigned to newly added particles based on a least squares approximation from neighboring particles. We refer to [25] for the algorithm of adding and removing particles. The total number of particles remains approximately the same throughout a simulation. This so-called particle management is needed for all time dependent flow problems. No-slip boundary conditions are applied at all solid walls. The initial contact angle of the liquid with the solid wall is 90^o. If the prescribed contact angle θ_s is different from the initial contact angle, the contact line moves and the liquid surface deforms to achieve the contact angle θ_s.

For $\theta_s = 175^o$ we initialize the region below the line $y = 0.02$ as liquid, the rest as gas, see Fig. 3(a), where blue (or dark gray) particles are liquid particles and red particles (or light gray) are gas particles. In Fig. 3 we have plotted the time evolution of the phase distribution. We observe that at around $t = 1.9s$ the liquid detaches from the solid wall after which it moves inside the gas. Then it forms an oscillating drop. The snapshots are comparable with the results published in the papers by Brackbill et al [4] and Liu et al [15].

Next, we consider the case of $\theta_s = 5^o$. In this case we choose the region below the line $y = 0.05$ to be the liquid domain, the rest of the domain is filled with gas. The time evolution of the two phases is plotted in Fig. 4. We observe that the liquid starts wetting the upper parts of the two side walls. At a time around $t = 2.4s$ the liquid reaches its maximum height and then starts oscillating. A similar behavior was observed in [4].

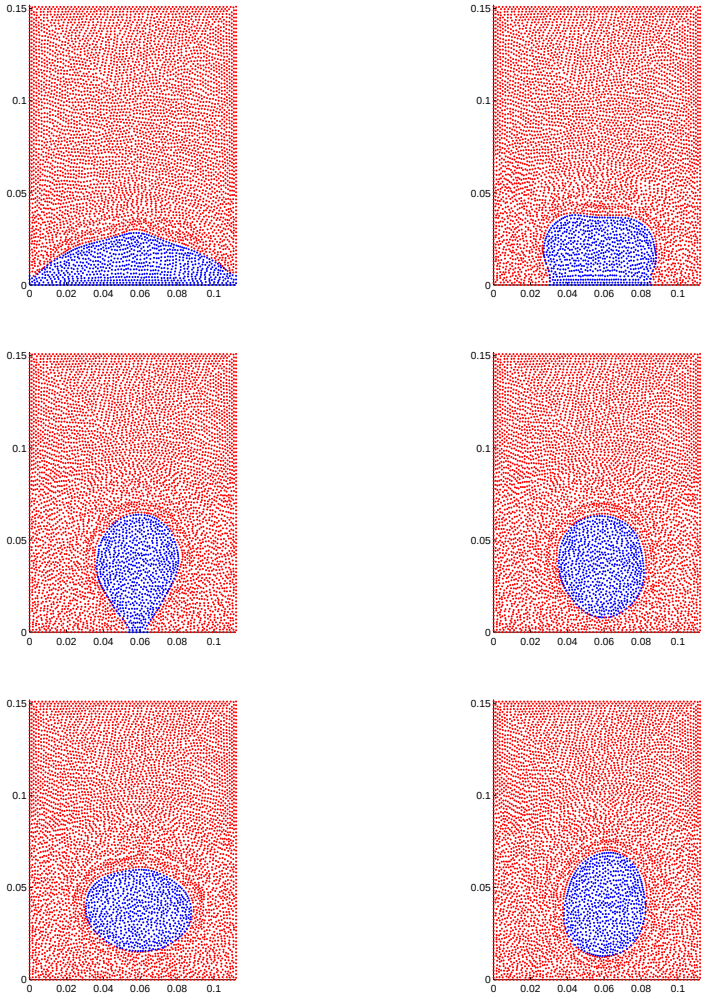

Figure 3: Time evolution of the two phases for $\theta_s = 175^o$. From left to right, first row: $t = 0.5$ s and 1.0 s, second row: $t = 1.8$s and 2.0 s, third row: $t = 2.4$s and 3.0 s. Blue (or dark gray) particles indicate liquid particles and red (or light gray) ones indicate gas particles.

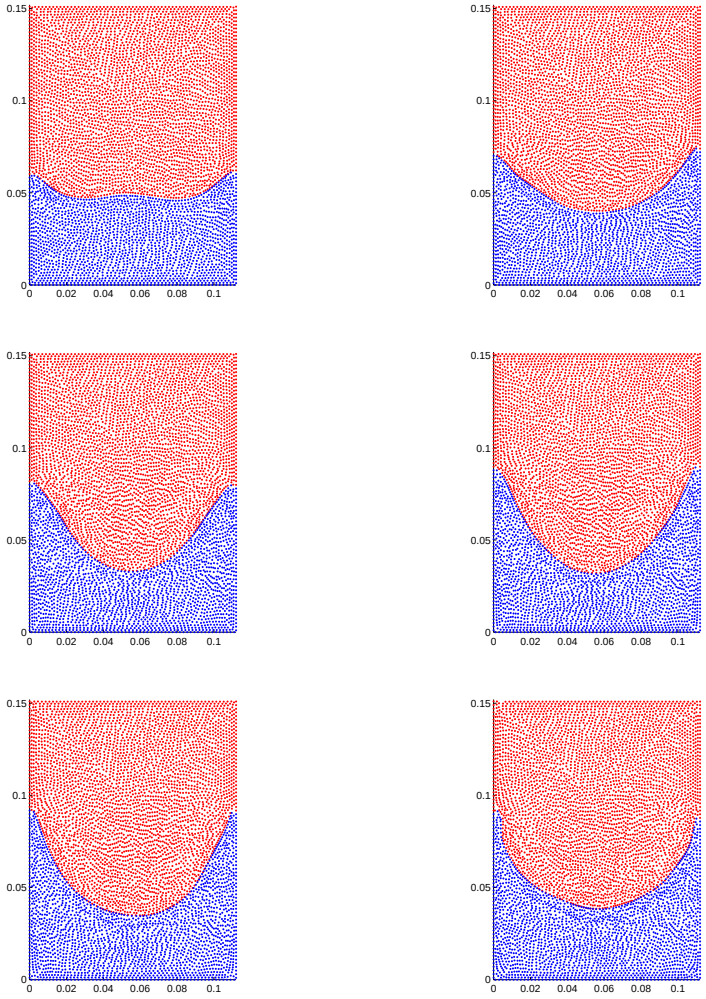

Figure 4: Time evolution of the two phases for $\theta_s = 5^o$. From left to right, first row: $t = 0.5$ s and 1.0 s, second row: $t = 1.5$s and 2.0 s, third row: $t = 2.4$s and 3.0 s. Blue (or dark gray) particles indicate liquid particles and red (or light gray) ones indicate gas particles.

4.3. Stationary shape of sessile drops

4.3.1. Drops without gravity

This test case is also taken from the paper by Liu et al [15]. Consider a two-dimensional domain $[0, 0.4] \times [0, 0.12]$. The initial spacing of the particles is defined via $\Delta x \approx h/3$ with $h = 0.005$. This gives an initial total number of particles equal to 6536. We consider an initially rectangular ethanol drop of size $[0.15, 0.25] \times [0, 0.06]$ at the bottom of the domain. If the initial particle positions lie inside this rectangle, we define them as liquid particles, otherwise as gas particles, see Fig. 5(a). The fluid parameters are same as in [15]. The ethanol drop has a density $\rho_l = 797.88$ kg m^{-3} and a viscosity $\mu_l = 0.0018$ Pa s. The surface tension coefficient is $\sigma = 0.02361$ N m^{-1}. The gas density is $\rho_g = 1$ kg m^{-3}. To dampen the drop oscillations, a large gas viscosity $\mu_g = 0.01$ Ps s is considered. Gravitational and other external forces are set to zero. The initial velocity of all particles is zero. We apply no-slip boundary conditions at all domain boundaries. We have studied five different static contact angles $\theta_s = 30^o, 60^o, 90^o, 120^o$ and 150^o. In Fig. 5 the stationary drop shapes are shown for all contact angles. These results are comparable with the results presented in Liu et al [15].

In order to verify the the computational results quantitatively, we consider a circular drop sitting at the bottom wall. We initialize an ethanol drop with radius R_0 as shown in Fig. 6. This type of drop was considered in [7].

First, we neglect external forces such as gravity. In a stationary state a circular drop with static contact angle θ_s will form a circular cap with spreading length L, height H, and radius of curvature R, as shown in Fig. 6. These parameters depend on the drop volume (i.e. area in 2D) and the static contact angle θ_s. The height and spreading length of the drop can be expressed as

$$H = R(1 - \cos\theta_s), \qquad L = 2R\sin\theta_s. \tag{43}$$

From simple geometrical considerations the area of the circular cap in Fig. 6 is given by

$$A = R^2\theta_s - R^2\sin\theta_s\cos\theta_s. \tag{44}$$

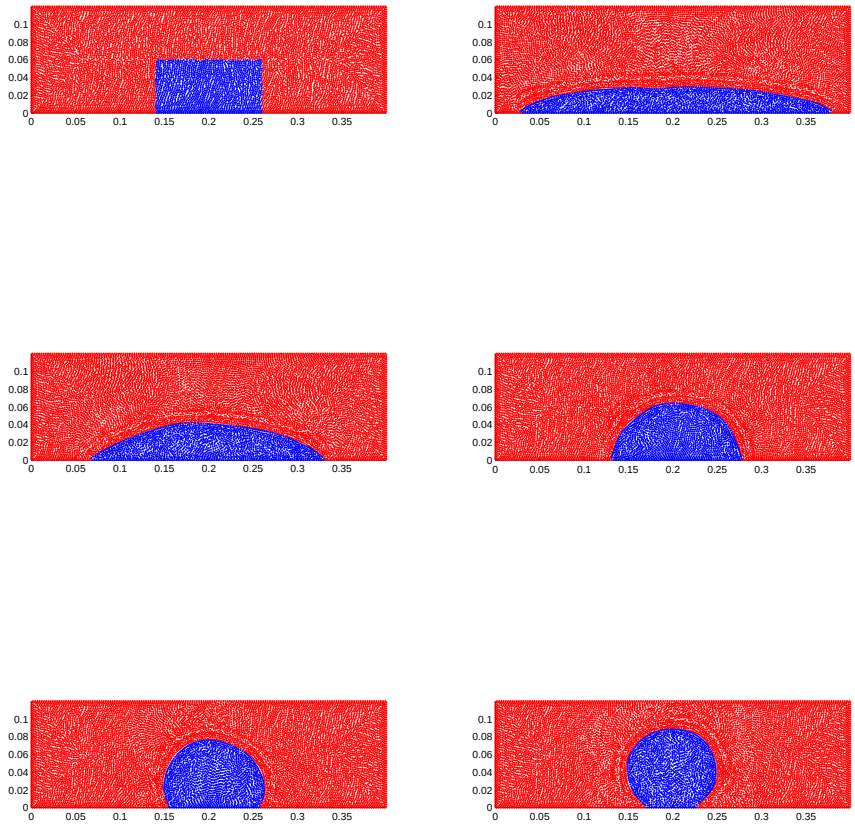

Figure 5: Initial shape and stationary shapes of sessile drops. From left to right, first row: initial drop and stationary drop for $\theta_s = 30^o$, second row: $\theta_s = 60^o$ and $\theta_s = 90^o$, third row: $\theta_s = 120^o$ and $\theta_s = 150^o$. Blue (or dark gray) indicate liquid particles and red (or light gray) indicate gas particles.

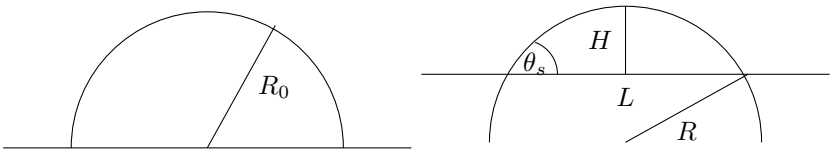

Figure 6: Initial (left) and final (right) shape of a circular drop.

Conservation of volume yields $A = \pi^2 R_0^2/2$. So the final radius of curvature is given by

$$R = R_0 \sqrt{\frac{\pi}{2(\theta_s - \sin\theta_s \cos\theta_s)}}. \tag{45}$$

Moreover, in steady state the Laplace law

$$\Delta P = \sigma / R \tag{46}$$

holds, where ΔP is the pressure difference between the surrounding gas and the liquid drop.

We consider a two-dimensional rectangular domain $[0, 0.3] \times [0, 0.123]$. We initialize liquid particles inside the semicircle of radius 0.06 and center $(0.15, 0)$, and gas particles in the rest of the domain. All fluid parameters are same as in the previous case with an initially rectangular drop except for the viscosities. We have considered larger viscosities such that the fluids reach their equilibrium states faster. Specifically, we have chosen $\mu_g = 0.01$ Pa s and $\mu_l = 0.1$Pa s. We consider five different static contact angles $\theta_s = 30^o, 60^o, 90^o, 120^o$ and 150^o. In Fig. 7 we plot the analytical circles according to (45) and the computed liquid distribution in the stationary state. The plots clearly show that the numerical results are very close to the analytical results.

Moreover, we plot the analytical spreading length and the height of the circular cap together with their numerical values in Fig. 8. The numerical value of the spreading length is computed as the difference of the x-coordinates of the extreme left and extreme right liquid particles. Similarly, the height is computed from the difference of the y-coordinates of the extreme top and extreme bottom liquid particles. The results show that for $\theta_s = 30^o$ it takes longer to converge to the analytical solution, however, for $\theta_s = 150^o$ the numerical solution reaches

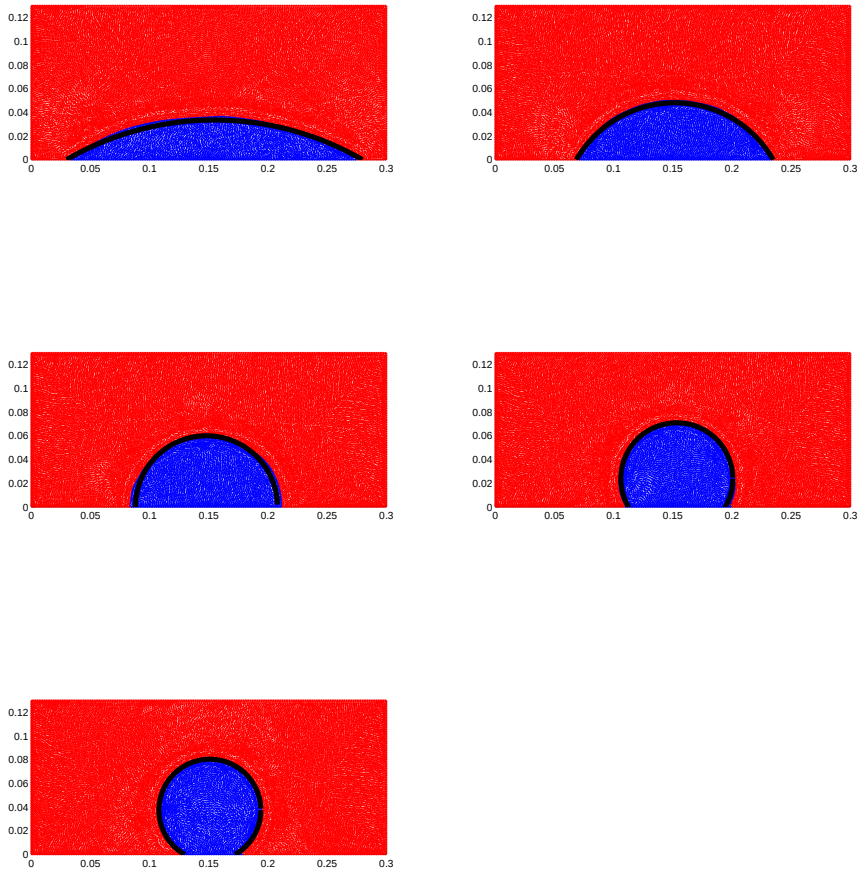

Figure 7: Stationary shapes of circular drops. From left to right, first row: for $\theta_s = 30^o$ and $\theta_s = 60^o$, second row: $\theta_s = 60^o$ and $\theta_s = 90^o$, third row: $\theta_s = 120^o$ and $\theta_s = 150^o$. The blue (or dark gray) indicate liquid particles, red (or light gray) indicate gas particles and the solid lines indicate the analytical circular shapes of liquid drops.

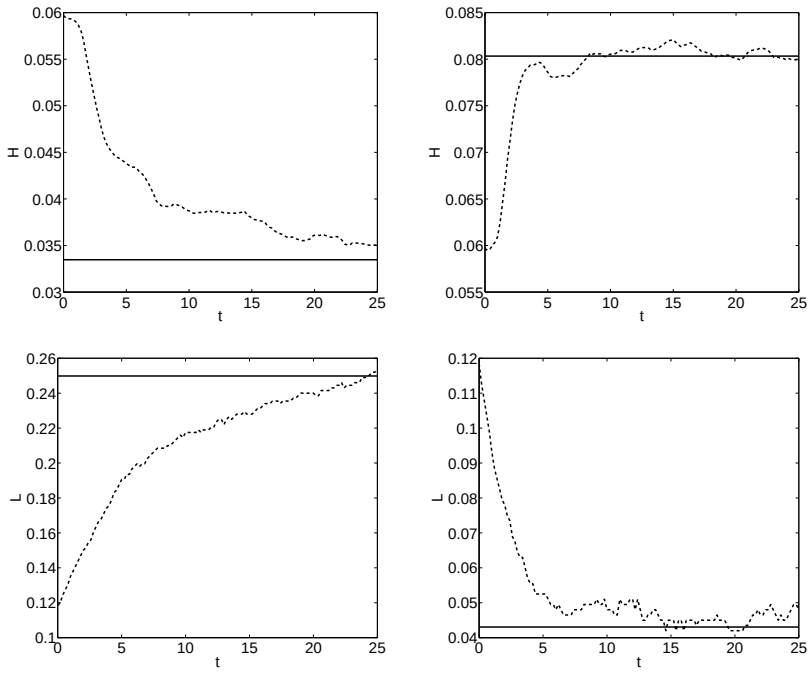

Figure 8: Time evolution of the drop spreading length L and the height H. The left figures are for $\theta_s = 30^o$, those on the right for $\theta_s = 150^o$. Solid lines represent the analytical solutions and dash lines represent the numerical solutions.

the stationary configuration after 5 seconds. Furthermore, we plot the Laplace law (46) in Fig. 9, giving quite satisfactory results. The pressure difference is calculated as the mean pressure of all liquid particles minus the mean pressure of all gas particles. To demonstrate the stability of the scheme, we have computed the kinetic energy inside the liquid drop. In Fig. 10 we see that after $t = 10s$ the kinetic energy remains small and stable.

4.3.2. Gravity effect

In this subsection we study the flattening of the drop due to gravity. In the absence of gravity the final shape of drop depends only on the static contact angle θ_s. When gravity is included, the shape also depends on the Eötvös number (Eo) defined by $Eo = \rho_l g R_0^2/\sigma$, where R_0 is the initial radius, g the

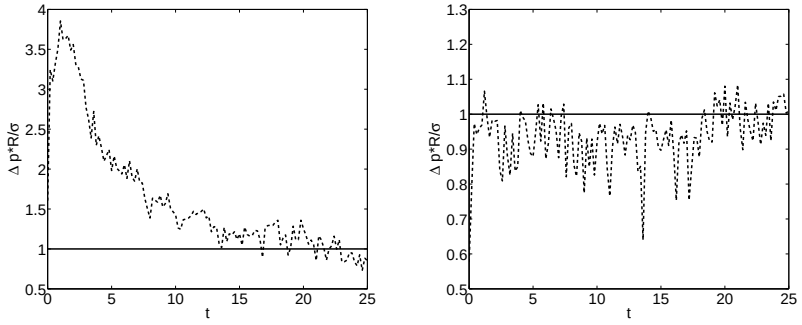

Figure 9: $\Delta p * \frac{R}{\sigma}$ versus time. The left figure is for $\theta_s = 30^o$, the right one for $\theta_s = 150^o$. Solid line represent the analytical solutions and dash lines represent the numerical solutions.

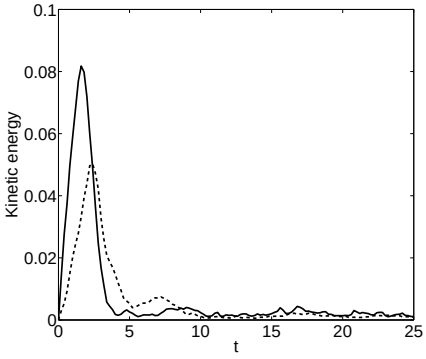

Figure 10: Kinetic energy versus time inside the drop. Dash line represents for $\theta_s = 30^o$ and solid line represents for $\theta_s = 150^o$.

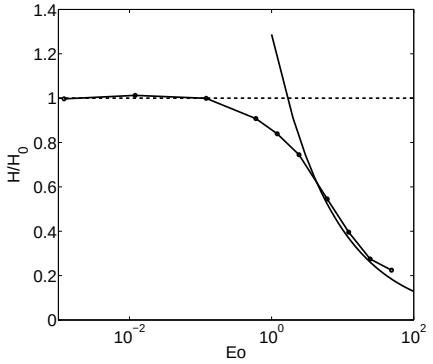

Figure 11: The ratio H/H_0 as a function of Eo for $\theta_s = 130^o$. Line with '-o-' represents the numerical results, dash line represents the result of Eq.(47), and the solid line represents the result of Eq. (48).

gravitational accelaration and ρ_l the liquid density. Sessile drops under gravity have been studied in [7], where the authors have computed the asymptotic shape of drops as a function of Eo. For $Eo << 1$ the shape is dominated by surface tension and the drop resembles a circular cap with angle θ_s. In this case the height of the drop can be reexpressed from (43) and (45) as

$$H_0 = R_0(1 - \cos\theta_s)\sqrt{\frac{\pi}{2(\theta_s - \sin\theta_s\cos\theta_s)}}. \tag{47}$$

For $Eo >> 1$ the shape of the drop is dominated by gravity and similar to a pancake whose height is directly proportional to the capillary length [7]

$$H_\infty = 2\sqrt{\frac{\sigma}{\rho_l g}}\sin(\frac{\theta_s}{2}). \tag{48}$$

We again consider an ethanol drop. All initial configurations and parameters are the same as in the previous test case 4.3.1, except for the contact angle θ_s. Here $\theta_s = 130^o$ is chosen in order to compare to the results presented in [7]. We change the Eötvös number by changing the gravitational acceleration, keeping the other parameters fixed. The gravity vector points in negative y direction. For the cases with $Eo > 12$ we have doubled the width of the computational domain which is now given by $[0, 0.6] \times [0, 0.123]$, since the length wetted by

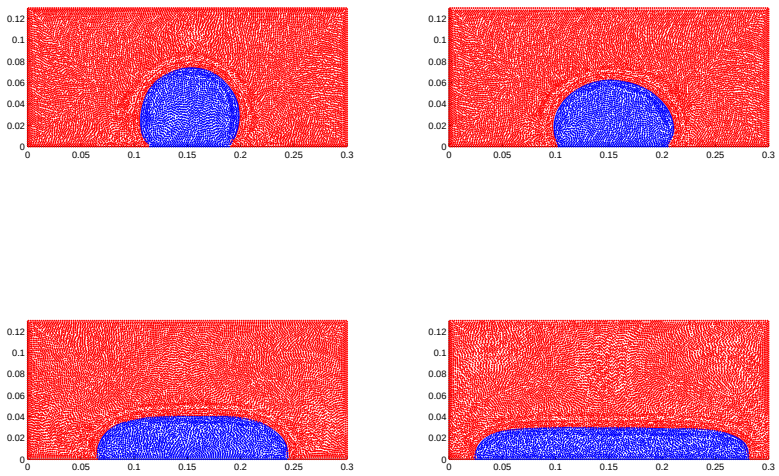

Figure 12: Final shapes of sessile drops for different Eötvös numbers and a static contact angle of $\theta_s = 130^o$, where red (or light gray) indicates gas particles and blue (or dark gray) indicates liquid particles. First row: $Eo = 0.12$ (left) and $Eo = 1.2$ (right). Second row: $Eo = 6.06$ (left) and $Eo = 12.16$ (right).

the droplet increases. Then the center of the drop is located at $(0.3, 0)$. As in the earlier case, we define the height H of the drop as the maximum value of the $y-$coordinates of all liquid particles. As can be seen in Fig. 8, the height and spreading length of the drop fluctuate around their analytical values. In order to obtain the height H as a function of Eo, we take the average value with respect to time. The averaging starts at $t = 4s$ and ends at the final time $t = 15s$. In Fig. 11 we show the numerical values of the ratio of H/H_0 as a function of Eötvös number together with the asymptotic solutions (47) and (48). The numerical and the asymptotic solutions agree very well. Like in the article by Dupont and Legendre [7], we also observe the transition between the circular cap and the pancake shape at around $Eo = 1$. In Fig. 12 we show the final shapes of the drop for varying Eötvös numbers.

4.4. Convergence study

In this section we study the numerical convergence. We consider an initially semi-circular drop sitting at the bottom wall, like in Fig. 6(a). The static contact angle is chosen as $\theta_s = 150^o$. We study three different values of the scale for the interaction radius in the particle method, $h = 0.1, 0.05$ and 0.0025. The corresponding initial numbers of particles are $2186, 8375$ and 32729, respectively. The other parameters are same as in subsection 4.3.1. In Fig. 13 we show the values of R, L and $\Delta p * R/\sigma$ as a function of time. One can observe convergence of the numerical solutions to the analytical ones when the number of particles increases. For $h = 0.05$ and 0.0025 there is not much difference in the height of the drop, but still significant differences in the spreading length and the Laplace pressure are visible between these two cases.

5. Concluding Remarks

We have presented a meshfree Lagrangian particle method to compute two-phase flows driven by wetting forces. The continuous surface force model is used to implement surface tension forces. The normal vector and the curvature of the fluid-fluid interface is computed with the help of a color function indicating the two phases based on a least-squares approach. All differential operators as well as the solution of the pressure Poisson equation are computed via the least-squares method. At the three-phase contact line between the two fluids and the solid wall the static contact angle is prescribed to model different wetting properties. The numerical results were compared with specific analytical solutions of a diffusion equation with phase-dependent diffusion coefficient. In addition to that, numerical test cases for wetting in a container as well as sessile drops with and without gravity were studied. Apart from a few exceptions where asymptotic analytical results are available, these cases can only be accessed numerically, but have been studied before by other authors. In all of the considered scenarios, a good agreement with the benchmark cases was obtained. Future work will be devoted to simulating dynamic wetting processes for which

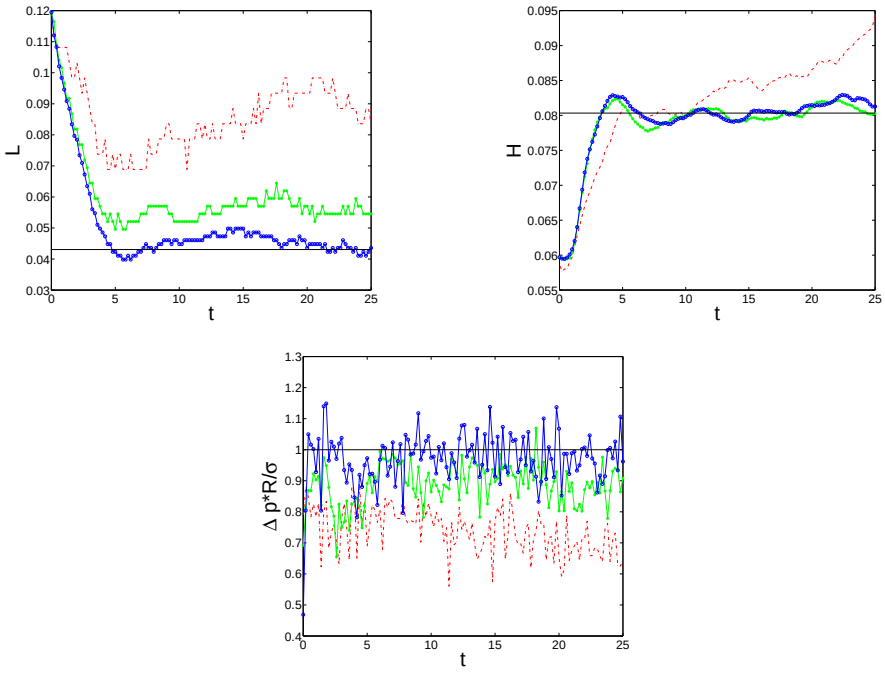

Figure 13: Time evolution of the drop spreading length L, height H and Laplace pressure for different numbers of particles and $\theta_s = 150^o$. Solid lines are analytical values, numerical solutions with red lines $-\cdot-$ are for $h = 0.01$, with green lines $-*-$ for $h = 0.005$ and with blue lines $-o-$ for $h = 0.0025$.

the dependence of the contact angle on the speed of the three-phase contact line will have to be modeled.

Acknowledgment

This work is partially supported by the German research foundation (DFG) grant number KL 1105/201. We would like to thank the DFG for the financial support.

References

[1] A. A. Amsden, The particle-in-cell method for the calculation of the dynamics of compressible fluids, Los Alamos Scientific Laboratory Report LA-3466, 1966.

[2] T. Babadagli, Dynamics of capillary imbibition when surfactant, polymer, and hot water are used as aqueous phase for oil recovery, J. Colloid Interface Sci. 246 (2002) 203213.

[3] T. Babadagli and Y. Boluk, Oil recovery performances of surfactant solutions by capillary imbibition, J. Colloid Interface Sci. 282 (2005) 162175.

[4] J. U. Brackbill, D. B. Kothe and C. Zemach, A continuum method for modeling surface tension, J. Comput. Phys., 100 (1992) 355-354.

[5] A. Chorin, Numerical solution of the Navier-Stokes equations, Math. Comput. vol. 22 (1968) 745-762.

[6] G.A. Dilts, Moving least squares particle hydrodynamics I, consistency and stability, Int. J. Numer. Meth. Engng., 44 (1999) 1115-1155.

[7] J. -P. Dupont, D. Legendre, Numerical simulation of static and sliding drop with contact angle hysteresis, J. Comput. Phys., 229 (2010) 2453-2478.

[8] M. A. Ebadian and C. X. Lin, A review of high-heat-flux heat removal technologies, J. Heat Transfer 133 (2011) 110801.

[9] R.A. Gingold, J.J. Monaghan, Smoothed particle hydrodynamics: theory and application to non-spherical stars, Monthly Notices Roy.Astronom. Soc. 181 (1997) 375389.

[10] C. W. Hirt, B. D. Nichols, Volume of fluid (VOF) method for the dynamics of free boundaries, J. Comput. Phys., 39 (1981) 201.

[11] F. H. Harlow, J. E. Welch, Numerical calculation of time-dependent viscous incompressible flow of fluid with free surface, Phys. Fluids 8 (1965) 2182.

[12] O. Iliev, S. Tiwari, A generalized (meshfree) finite difference discretization for elliptic interface problems, Springer Lecture Notes in Computer Sciences, vol. 2542, Springer, Berlin, 2003.

[13] S. Koshizuka, A. Nobe, Y. Oka, Numerical analysis of breaking waves using the moving particle semi-implicit method, Int. J. Numer. Meth. Fluids, 26 (1998) 751-769.

[14] J. Kuhnert, An upwind finite pointset method for compressible Euler and NavierStokes equations, (M. Griebel and M. A. Schweitzer, eds.), Lecture Notes in Computational Science and Engineering, vol. 26, Springer, 2002.

[15] J. Liu, S. Koshizuka, Y. Oka, A hybrid particle-mesh method for viscous, incompressible, multiphase flows, Comput. Phys., 202 (2004) 65-93.

[16] T. Liszka, J. Orkisz, The finite difference method on arbitrary irregular grid and its application in applied mechanics, Comput. & Structures 11 (1980) 8395.

[17] J.J. Monaghan, Simulating free surface flows with SPH, J. Comput. Phys. 110 (1994) 399.

[18] J. Monaghan and J. C. Lattanzio, A refined particle method for astrophysical problems, Astron. Astrophys. 149 (1985) 135143.

[19] J. P. Morris, Simulating Surface Tension with Smoothed Particle Hydrodynamics, Int. J. Numer. Methods Fluids, 33 (2000) 333-353.

[20] R. Seemann, M. Brinkmann, T. Pfohl and S. Herminghaus, Droplet based microfluidics, Rep. Prog. Phys. 75 (2012) 016601.

[21] M. Sussman, P. Smereka, and S. Osher, A level set approach for computing solutions to incompressible two-phase flow, J. Comput. Phys. 114 (1994) 146.

[22] A. B. Theberge, F. Courtois, Y. Schaerli, M. Fischlechner, C. Abell, F. Hollfelder, and W. T. S, Huck, Microdroplets in microfluidics: An evolving platform for discoveries in chemistry and biology, Angew. Chem. Int. Ed. 49 (2010) 58465868.

[23] S. Tiwari, J. Kuhnert, Grid free method for solving poisson equation, Wavelet Analysis and Applications, New Age International Publishers (2004) 151 - 166.

[24] S. Tiwari, J. Kuhnert, Finite pointset method based on the projection method for simulations of the incompressible Navier-Stokes equations, (M. Griebel and M. A. Schweitzer, eds.), Lecture Notes in Computational Science and Engineering, vol. 26, Springer, 2002, pp. 373–387.

[25] S. Tiwari, J. Kuhnert , A meshfree method for incompressible fluid flows with incorporated surface tension, revue aurope'enne des elements finis, Volume 11-n 7-8/2002 (Meshfree and Particle Based approaches in Computational Mechanics).

[26] S. Tiwari, J. Kuhnert, Modeling of two phase flows with surface tension by Finite Pointset Method (FPM), J. Comput. Appl. Math, 203 (2007) 376-386.

[27] S. Tiwari, A. Klar and S. Hardt, A particle-particle hybrid method for kinetic and continuum equations, J. Comput. Phys., 228 (2009) 7109-7124.

[28] S. O. Unverdi, G. Tryggvson, A front tracking method for viscous, incompressible, multi-fluid flows, J. Comput. Phys., 100 (1992) 25.

[29] S. J. Weinstein and K. J. Ruschak, Coating flows, Annu. Rev. Fluid Mech. 36 (2004) 2953.